Finite Element Simulation and Experimental Study on Vibration Characteristics of Converter Transformer Under DC Bias

Hao Wang, Li Zhang, Youliang Sun, and Liang Zou

***Abstract*—To clarify the electromagnetic, vibration, and loss characteristics of the internal components of a converter transformer under DC bias conditions and their influencing mechanisms, a series of studies are conducted using the finite element method and model experiments. This paper quantifies the influence of different DC contents on the magnetic flux density, force, and displacement distribution characteristics of the iron core and winding and analyzes the internal relationship between various indicators. The inflection point of the DC bias coefficient on the vibration is obtained and the contribution mechanism of the different responses of the iron core and winding to this inflection point is explained. The value of the DC bias coefficient for changing the main vibration frequency is determined. When the DC bias coefficient is 1.0 and 1.5, the main frequency of vibration moves to the right to 250 Hz and 350 Hz. Based on the principle of similarity, a DC bias vibration experimental platform for converter transformers is developed, and DC bias magnetic experiments are conducted to verify the reliability of the simulation results.**

***Index Terms*—DC bias, converter transformer, finite element and experimental analysis.**

I. Introduction

As the core large-scale power equipment in high-voltage direct current (DC) engineering, the safe and stable operation of converter transformers is directly related to the power quality and the safe and stable operation of ultra-high-voltage transmission [1]–[9]. The operation of a converter transformer is accompanied by a high transmission voltage and numerous DC and harmonics, resulting in special electromagnetic and vibration characteristics [10]–[12]. In particular, the DC bias effect can easily result in rapid unidirectional saturation of the core, resulting in local overheating, vibration, noise, and even operational accidents [13], [14]. Scholars have conducted effective research on the DC bias problem in transformers. Reference [15] designs a passive negative reluctance structure that can effectively suppress the influence of DC bias through a bandpass filter with variable frequency reluctance characteristics, but the structure is only suitable for small capacity transformers. Reference [16] studies the effect of DC bias on zero sequence impedance of 220 kV transformers, and proposes a relay friendly capacitive isolation method to suppress the DC bias in 220 kV transformers. Reference [17] designs a magnetoresistive model to analyze the impact of DC bias on the loss factor of three-phase five column transformers and provides the law of the impact of DC bias on the maximum load capacity of the transformer. From the above research cases, it can be observed that owing to the high working voltage and cost of converter transformers, relatively little research exists on the vibration and loss characteristics of converter transformers under DC bias conditions. The mechanism of the impact of the DC bias on the vibration and loss of the internal components of converter transformers requires further quantitative research [18].

The mature application of finite element technology has brought great convenience to the electromagnetic and multifield coupling simulation of high-power equipment, providing an experimental platform for conducting and verifying experiments that are difficult to perform in practical engineering applications [19], [20]. In [21], a three-dimensional finite element analysis model is established for power transformers, which simulates the effect of shielding on stray loss distribution using the surface impedance method, and obtains the temperature field distribution characteristics of the rising flange based on the magneto thermal coupling method. Reference [22] conducts simulation experi-

Received: August 1, 2023
Accepted: May 10, 2024
Published Online: July 1, 2024
Hao Wang, Li Zhang (corresponding author), and Liang Zou are with the School of Electrical Engineering, Shandong University, Jinan 250061, China (202120603@mail.sdu.edu.cn; zhleee@sdu.edu.cn; zouliang@sdu.edu.cn)
Youliang Sun is with the School of Electrical Engineering, Shandong University, Jinan 250061, China; and Shandong Power Equipment Co., Ltd., Jinan 250101, China (201920495@mail.sdu.edu.cn)
DOI: 10.23919/PCMP.2023.000034

ments using the finite element method (FEM) and proposes a method for calculating the DC bias voltage using the reactive power loss of the converter transformers. The reactive power loss is quantified and the feasibility of the algorithm is verified. However, the design of most converter transformer models has shortcomings, particularly in terms of the winding mode, distribution of support buffer blocks, and differences between various components of the winding, which are crucial for the performance of winding vibration characteristics [23]–[25].

This paper uses FEM to optimize the design of a full-size model of the electric-magnetic-force multi-field coupling of the converter transformer based on the design and operating parameters provided by the manufacturer of the converter transformer. A comprehensive analysis is conducted on the impact of the DC bias on the electromagnetic, loss, and vibration characteristics of converter transformers, and the coupling relationship between the electromagnetic, force, and loss characteristics of converter transformers under a DC bias is clarified. An experimental DC bias platform for converter transformers is designed and constructed based on the similarity principle. By testing the vibration characteristics under a DC bias, the effects of different DC components on their main frequency, waveform, and amplitude are quantitatively analyzed. Finally, based on the conclusions of this paper, suggestions for the design and operation of converter transformers are proposed.

II. DC Bias Effect

The DC magnetic bias effect is caused by the abnormal working state of the converter transformer core. Its occurrence conditions may include an imbalance in the trigger angle of the converter valve, earth circuit operation of the DC transmission system, and solar storms, which can be explained by the nonlinear magnetization curve under the condition of core saturation. The excitation characteristic curve and measured current waveform change when a DC current is introduced into the converter transformer winding are depicted in Fig. 1.

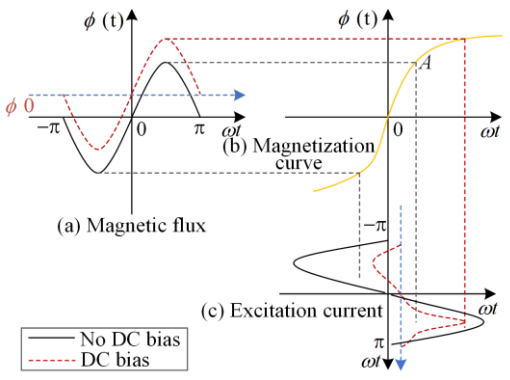

Fig. 1. Mechanism of DC magnetic bias.

The solid line shown in Fig. 1 (a) represents the magnetic flux curve under normal excitation conditions, and the dotted line represents the magnetic flux curve with the DC component. Figure 1 (b) illustrates the nonlinear excitation curve, the *OA* section is the linear working area, the *AB* section is the saturated working area, and the real and dotted lines in Fig. 1 (c) show the excitation current waveform curves under normal conditions and in the presence of DC, respectively. In the design of the magnetic circuit of a converter transformer, the working point of the ferromagnetic material is often located near the knee point to obtain a larger magnetic flux with a smaller magnetomotive force. The main flux operates at point *A* at the end of the linear zone under the rated working conditions. When the DC current enters the converter transformer winding, a DC magnetic flux offset is generated, and the AC and DC magnetic fluxes overlap, causing the magnetic flux curve to deviate from the time axis. The operating point of the converter transformer moves from the unsaturated region of the magnetization curve to the nonlinear region at the end, where it is in a half wave saturated state. Thus, the excitation current is distorted, and the peak value in the half cycle in the same direction as the DC magnetic bias increases, whereas the other half cycle gradually decreases to zero. The positive and negative half waves of the excitation current are asymmetric, and odd and even harmonic components are generated.

III. Modeling

Based on the structure and operating parameters of the ±500 kV operating converter transformer (ZZDFPZ-415000/500-800) provided by Shandong Electric Power Equipment Co., Ltd., a three-dimensional physical model of the electric magnetic force multi field coupling of the converter transformer is established, as shown in Fig. 2. This paper aims to elucidate the mechanism of the influence of the DC bias on the electromagnetic and vibration characteristics inside converter transformers, including the coupling relationship between them. This requires distinguishing the model design from general simplified models in previous studies [20]–[22]. The transformer models used in these studies and analyses typically simplify the iron core into a combination of fully connected cylinders, and the windings are concentric circular cylinders. This makes geometric modeling easy to implement but is only applicable to the study of electromagnetic field distribution characteristics. It is difficult to accurately reflect the mechanical characteristics of transformers when studying the coupling between electromagnetic fields and solid mechanics. The coupling of electromagnetism and vibration originates from the electric force of the winding under an alternating current and the magnetostriction of the iron core under an alternating magnetic field. Considering the winding as an example, the spa-

tial distribution of the electric field and electric force received by the spiral-structure winding and continuous-type winding are completely different, and the structure of the model determines its modal shape, which greatly affects the final vibration form. Therefore, when designing a winding, the winding should be as consistent with the actual structure as possible.

TABLE I
MEASUREMENT PARAMETERS OF 23RK085 SILICON STEEL SHEET

B (T)	*I* (A/m)	*B* (T)	*I* (A/m)	*B* (T)	*I* (A/m)
0.499	9.4	1.577	29.1	1.747	58.8
0.599	10.5	1.587	29.8	1.757	63.5
0.698	11.7	1.597	30.6	1.766	67.9
0.799	12.8	1.608	31.4	1.776	73.9
0.898	14.0	1.616	32.2	1.786	80.6
0.998	15.2	1.626	33.2	1.796	89.0
1.097	16.2	1.637	34.3	1.806	98.8
1.197	17.7	1.647	35.6	1.815	108.5
1.297	19.5	1.657	36.9	1.826	121.9
1.398	21.8	1.666	38.2	1.836	138.4
1.497	25.0	1.677	39.9	1.846	157.8
1.516	25.8	1.687	41.7	1.857	182.1
1.526	26.3	1.696	43.7	1.865	207.3
1.537	26.8	1.707	46.1	1.875	244.6
1.547	27.4	1.716	48.4	1.886	291.6
1.558	27.9	1.726	51.4	1.896	350.3
1.566	28.4	1.736	54.9		

The overall approach of this paper for model design is to balance computational accuracy and efficiency, simplify structures that are weakly related to the topic, and strengthen the precision and rationality of the main research objects for research purposes. Fans and insulation support materials with relatively small DC bias effects are simplified, and the main role of the DC bias effect is to restore the structure of the iron core and winding as much as possible. The iron core design adopts a six-step lamination form for overlap with a 9-level iron core lamination structure that decreases in size and area from the middle iron core level to both sides. An oriented, pressed silicon steel sheet (model 23RK085) is used as the iron core material. The measurement parameters of this type of silicon steel sheet are sequentially imported into the *H-B* curve node of the iron core material to restore the working characteristics of the iron core. The magnetic characteristics of this type of silicon steel sheet are listed in Table I. The winding is designed as a structure with tangled ends on the high-voltage side, a continuous middle, and an overall spiral on the low-voltage side. The advantage of using an entangled type at the end of a high-voltage winding is that when the surge voltage invades the transformer type, and the voltage is often concentrated at the end of the winding, which is known as the end effect. This structure can effectively improve the uniform distribution of voltage and reduce the impact of the surge voltage on the winding. An epoxy resin cushion block structure is installed between the cake and the cake of the high-voltage side winding to simulate the supporting vibration reduction structure between the actual winding cakes. The fuel tank is composed of ordinary structural steel, and the surfaces of the front and back fuel tanks are replaced with rectangular steel plates of the same material as the reinforcing rib structure. The material parameters of the model are listed in Table II.

TABLE II
MATERIAL SETTINGS FOR FINITE ELEMENT MODEL COMPONENTS

Name	Core	Winding	Spacer	Insulating oil	Air
Density (kg/m^3)	7870	8940	1120	901	1.29
Young's modulus (GPa)	5.8	13.1	1		
Poisson's ratio	0.46	0.35	0.39		0
Conductivity (S/m)	1.13×10^7	5.98×10^7	1	1	1
Relative permittivity	1	1	1		1

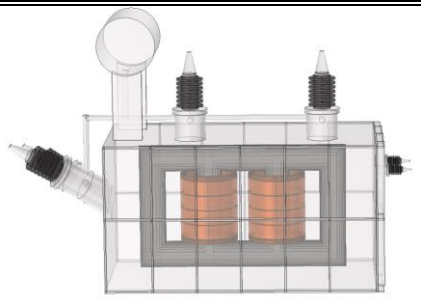

Fig. 2. Multiphysics simulation coupled finite element simulation platform for converter transformer.

Figure 3 (a) describes the principle of "field circuit coupling." Figure 3 (b) gives the injection method of DC current, where R_1 and R_2 represent internal resistance, I/U represents the winding coil admittance, AC and DC represent the AC source sequence and DC source sequence, respectively. Upon connecting to the DC power supply, the circuit still satisfies the transformer voltage equations (1) and (2). The harmonic data contained in the AC power supply originate from the on-site collection of the operating converter transformer; the specific data are presented in Table III, and the design details of the winding structure are shown in Fig. 3 (c).

$$u_1 = i_{10}R_1 - e_1 = i_{10}R_1 + N_1\frac{\mathrm{d}\phi}{\mathrm{d}t} \tag{1}$$

$$u_{20} = e_2 = -N_2\frac{\mathrm{d}\phi}{\mathrm{d}t} \tag{2}$$

where u_1, i_{10}, i_{10}, e_1, and N_1 denote the primary voltage, current, resistance, electromotive force, and turns of the transformer, respectively; and u_{20}, e_2, and N_2 denote the secondary voltage, electromotive force, and turns, respectively.

TABLE III
ACTUAL COLLECTION OF HARMONIC FREQUENCY AND CONTENT OF CONVERTER TRANSFORMERS

Harmonic order	Frequency (Hz)	Amplitude (A)	Harmonic order	Frequency (Hz)	Amplitude (A)
5	250	708.26	29	1450	27.32
7	350	447.06	31	1550	23.13
11	550	184.81	35	1750	17.24
13	650	119.40	37	1850	15.82
17	850	62.01	41	2050	14.38
19	950	47.84	43	2150	13.56
23	1150	41.27	47	2350	10.92
25	1250	37.66	49	2450	9.56

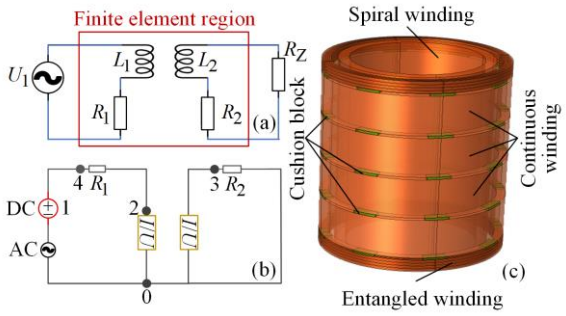

Fig. 3. Coupling circuit. (a) Field circuit coupling principle. (b) DC circuit diagram. (c) Overall structure of winding.

The multi field coupling finite element calculation of converter transformers is used to solve the equation for the changes in the internal operating parameters of converter transformers over time and space, including the electromagnetic field and solid mechanics at any finite element point, as well as the coupling effect between them, to experimentally solve the problem of unobservable physical phenomena.

The finite element dynamic equation of winding and iron core structure is:

$$\boldsymbol{M}\ddot{s}(t)+\boldsymbol{C}\dot{s}(t)+\boldsymbol{K}s(t)=\boldsymbol{Q}(t) \tag{3}$$

where $\ddot{s}$ and $\dot{s}$ represent the node acceleration and velocity vectors, respectively; $\boldsymbol{M}$ denotes the mass matrix of the model; $\boldsymbol{C}$ represents the damping matrix of the model; $\boldsymbol{K}$ represents the stiffness matrix; and $\boldsymbol{Q}$(t) represents the load vector. Ignoring the influences of damping and external forces, the above equation can be further simplified as:

$$\boldsymbol{M}\ddot{s}+\boldsymbol{C}\dot{s}(t)=0 \tag{4}$$

This is the free vibration equation of the system and is also known as the dynamic characteristic equation. Using this equation, the natural frequencies and vibration modes of the system can be solved.

Under the alternating magnetic field generated by the alternating current, the winding is subjected to a radial electric force F_x and an axial electric force F_z generated by the axial and radial magnetic flux leakages:

$$F_x=iB_{zt}\cdot 2\pi r \tag{5}$$

$$F_z=iB_{xt}\cdot 2\pi r \tag{6}$$

The vibration model of silicon steel sheet under alternating magnetic field is

$$D_0\left(\frac{\partial^4 v}{\partial x^4}+2\frac{\partial^4 v}{\partial x^2\partial y^2}+\frac{\partial^4 v}{\partial y^4}\right)=\frac{\omega\sin 2\omega t}{\Delta l_x}\int_v\frac{1}{2}E\lambda_z^3\mathrm{d}V \tag{7}$$

where D_0 denotes the bending stiffness of the silicon steel sheet; v is the Poisson's ratio of the material; x and y indicate the transverse and longitudinal dimensions of two-dimensional silicon steel sheet, respectively; ω denotes the angular frequency; t is the time; l_x denotes the elongation; E indicates the elastic modulus of the material; λ_z is the axial magnetostriction coefficient; and V indicates the volume element.

Currently, the gaps between the silicon steel sheets in the iron cores used in converter transformers are becoming increasingly smaller, and the stacking method is becoming more advanced. The Maxwell stress between the silicon steel sheets can be ignored; therefore, the main contribution of the iron core vibration is the magnetostrictive effect of ferromagnetic materials under alternating electric fields. The magnetostrictive force caused by the magnetostrictive effect in the parallel and vertical directions can be expressed as:

$$F_c=F_{c\max}\sin 2\omega t=0.5\nabla(H^2\tau\partial\frac{\partial\mu}{\partial\tau}) \tag{8}$$

where F_c signifies the magnetostrictive force; $F_{c\max}$ denotes the amplitude of the electromagnetic force caused by magnetostriction; and μ is the magnetic permeability.

TABLE IV
NATURAL FREQUENCIES OF WINDINGS AND CORES

	Natural frequency					
Winding (Hz)	77.46	134.55	178.76	250.83	291.62	352.01
Core (Hz)	77.53	128.78	164.64	247.79	288.62	349.78

The model mode shape of the converter transformer reflects its inherent structural vibration form, and the characteristic frequency distribution of the model can be solved using (2), regardless of the external excitation. In the finite element software, only the geometry, material, and solid mechanics are considered separately, and modal calculation is performed on the winding and core to obtain their natural frequencies. Table IV lists the first six natural frequencies with the most significant vibrations of the model. When designing converter transformers, it is usually necessary to consider whether the main mode resonates at a possible excitation frequency. The distribution of each mode of the converter transformer model established in this paper is designed reasonably [26]. Based on the principle of field-circuit coupling, different DC components of different sizes are applied to the model winding, and DC bias experiments are simulated. The DC component content is determined using the DC bias coefficient, which is defined as the ratio of the peak DC current to the peak no-load current. The DC bias coefficients used in the DC bias simulation experiments are 0, 0.5, 1.0, and 1.5.

IV. ANALYSIS OF SIMULATION RESULTS

Previous research has typically focused on the effects of DC bias on electromagnetic characteristics, such as excitation current, spatial magnetic field strength, losses, and harmonics, which are the most direct and easily observable characteristics of DC bias [29], [30]. How-

ever, few scholars have fully considered the electromagnetic, vibration, and loss characteristics of the DC bias, including their mutual influence. The DC bias is not simply an electromagnetic disturbance problem. It presents many negative effects, such as increased noise, increased losses, and a shift in operating characteristics. However, explanations for these physical phenomena have rarely been studied. The interior of a converter transformer is a complex and massive electromagnetic system, and all internal components constitute and affect the system. Therefore, it is not only necessary to analyze them separately, but also to analyze the coupling relationship between them to systematically explain the mechanism of DC bias on the overall effect of the converter transformer. Figures 4(a)–(d) depict the force distribution of the core at each K_{dc} value. As the DC component increases, the distribution range of the stress on the core widens, and the distribution of the stress application points becomes more disordered. As the K_{dc} increases from 0 to 1.0, the force of the core increases from 3.12×10^5 Pa to 2.37×10^6 Pa. Magnetostriction refers to the extension or shortening of magnetic domains in the magnetization direction of silicon steel sheets [27], [28]. However, as K_{dc} increases from 1.0 to 1.5, the rate of increase in the force on the core decreases sharply. This is because K_{dc} is approximately 1.0, the core approaches saturation, and it is close to the flat area of the hysteresis loop. Table V summarizes the changes in the magnetic flux density, force, displacement, and loss parameters of the core and winding for different K_{dc}.

Figures 4 (e) and (f) show the displacement distribution characteristics of the core for different DC contents, and their displacements correspond to the force distribution. The deformation characteristics exhibit two completely different forms, before and after an increase in the DC component. When K_{dc} is 0, the deformation amplitude of the core is 2.56×10^{-8} m, and when K_{dc} is 0.5, 1.0, and 1.5, the deformation amplitude increases to 7.41×10^{-8} m, 2.33×10^{-7} m, and 3.12×10^{-7} m, respectively. Although the DC bias exacerbates core vibration, the overall form of the deformation distribution remains unchanged. However, the DC bias magnetization increases the force at some points in the core, particularly at the junction of the main column and upper yoke, causing changes in the deformation characteristics of the core at this point after increasing the DC component. As the core approaches saturation, the distortion becomes more pronounced; this simulation result is consistent with the conclusion of [31].

TABLE V
MAGNETIC FLUX DENSITY, FORCE, DISPLACEMENT, AND LOSS PARAMETERS AT DIFFERENT K_{DC}

K_{dc}	Magnetic flux density (T)	Core stress (Pa)	Winding stress (Pa)	Core deformation (m)	Winding deformation (m)	Core loss density (W/m^3)	Winding loss density (W/m^3)
0	1.52	3.12×10^5	1.29×10^5	2.56×10^{-8}	1.43×10^{-7}	42 069	10 541
0.5	1.58	8.38×10^5	4.68×10^5	7.41×10^{-8}	5.12×10^{-7}	45 538	16 383
1.0	1.72	2.37×10^6	7.31×10^5	2.33×10^{-7}	8.33×10^{-7}	58 708	18 593
1.5	1.76	3.76×10^6	5.47×10^6	3.12×10^{-7}	2.86×10^{-6}	73 446	19 768

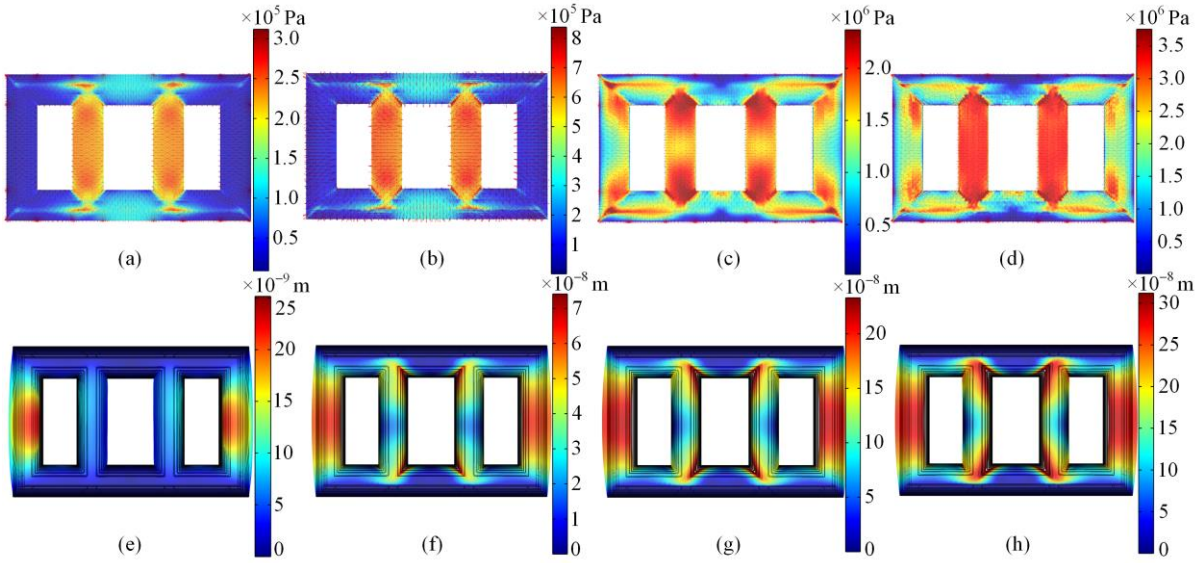

Fig. 4 Force and displacement distribution of iron core under different DC contents. (a)–(d) Stress distribution and displacement distribution. (e)–(f) Characteristics of core under different DC components.

Figure 5 summarizes the loss characteristics, force displacement, and magnetic flux loss relationships of the core and winding for different K_{dc} values. It can be observed from Fig. 5 (a) that the overall change trend of the force on the core and the displacement is consistent, but after K_{dc} reaches 1.0, the rate of increase of the core displacement decreases, which is contrary to the experience. We believe that the vibration and noise of converter transformers will increase significantly after the core is saturated, which should be reflected in the displacement of internal components at the micro level [32]. A possible explanation here is that after the core is saturated, the increase in harmonics makes the natural frequency of the converter transformer body coincide with it, thus generating overall resonance and increasing the overall noise of the converter transformer, rather than originating from the core alone.

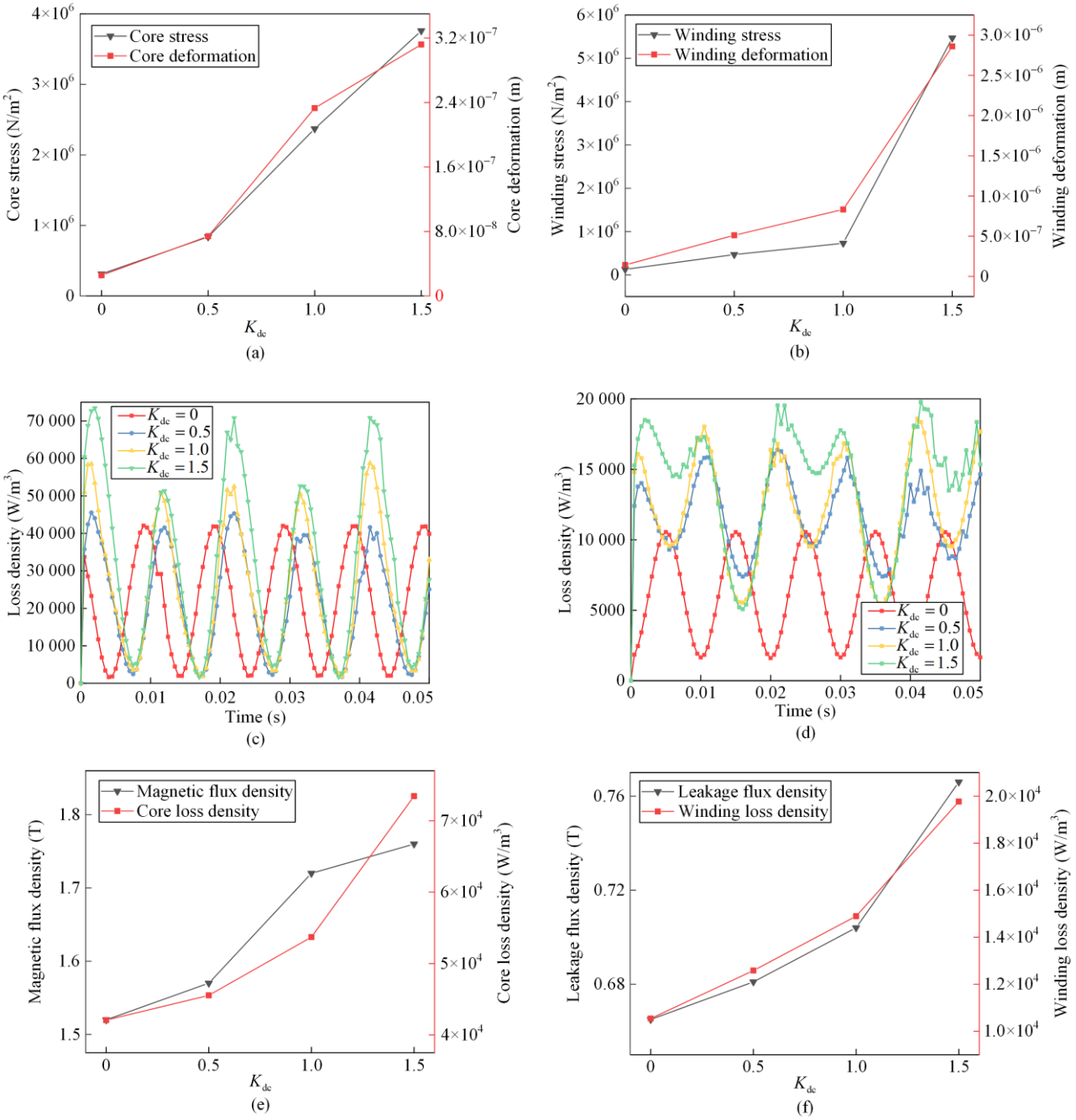

Fig. 5. Variation relationship between parameters under different DC contents. (a)–(b) Force displacement relationship. (c)–(d) Loss characteristics. (e)–(f) Magnetic flux loss relationship under different K_{dc}.

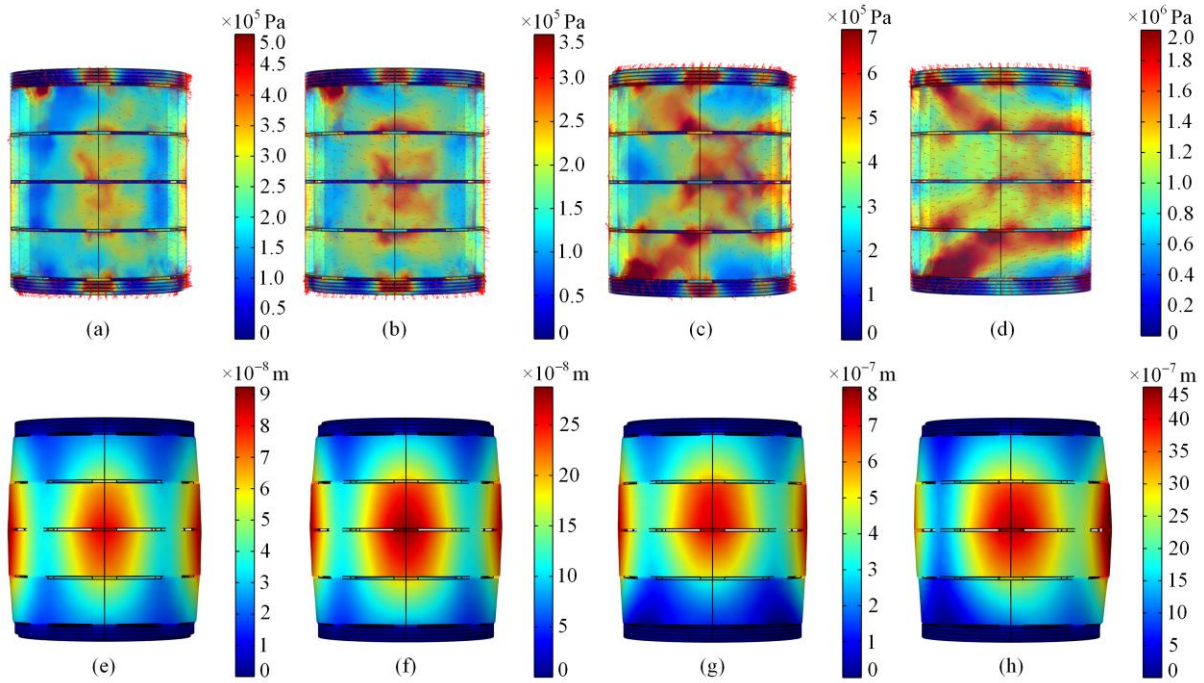

Fig. 6. Force and displacement distribution of windings under different DC contents. (a)–(d) Stress distribution. (e)–(f) Displacement distribution characteristics of windings under different DC components.

Figures 6 (a)–(d) depict the force characteristics of the windings at each K_{dc}. As K_{dc} increases from 0 to 1.5, the force amplitude of the winding increases from 1.29×10^5 Pa to 5.47×10^6 Pa, based on (16) and (17), which is related to the current and magnetic flux leakage. As the DC offset coefficient increases, the direction of force at each point of action of the winding does not change much, but the distribution of force on the winding changes, and the distribution range of force intensity points increases. Under the action of DC bias, the magnetic flux density increases, increasing the established leakage flux density value. Once the core saturates, the loss of the core increases, which is reflected in the increase in magnetic flux density on the winding, oil tank, and fixture. Concurrently, after the core is saturated, harmonic currents are generated, which act on different force points of the winding at different angular frequencies. From Figs. 6 (e)–(f), it can be observed that the displacement amplitude of the front core without adding a DC source is 1.4×10^{-7} m. At K_{dc} is 0.5, 1.0, and 1.5, the maximum winding displacement increases to 5.12×10^{-7} m, 8.33×10^{-7} m, 8.33×10^{-7} m, and 2.86×10^{-6} m, respectively. It can be observed from Figs. 5 (e)–(f), with the increase of K_{dc}, the change trend of winding shape variable and stress is basically consistent, which is different from that of core. Upon reaching the saturation point of the core, the leakage magnetic flux increases significantly, which acts on the displacement distribution of the winding and increases the displacement amplitude of the winding.

Figures 5 (c)–(d) describe the loss characteristics of converter transformers at different K_{dc} values. As the K_{dc} increases from 0 to 1.5, the core loss increases from 4 2069 W/m^3 to 7 3446 W/m^3. Specifically, after the K_{dc} is greater than 1.0, the core loss sharply increases, which corresponds to harmonic and eddy current losses after the core is saturated. The leakage magnetic loss characteristics of the winding are relatively synchronous, as shown in Figs. 5 (e)–(f). The K_{dc} increases from 0 to 1.5, and the winding loss increases from 10 541 W/m^3 to 19 768 W/m^3. At a K_{dc} of 1.0, the magnetic flux density loss characteristics of core and winding undergo different changes, reflecting the different ways in which DC bias affects the core and winding. In addition to the influence of its own electrodynamic force, the vibration and loss characteristics of the winding vary with the operating characteristics of the iron core, which depend on the changes in the movement trajectory of electrons in the vertical leakage direction of the winding [33].

Figures 7 (a) and (b) illustrate the vibration acceleration spectra at the centers of the core and winding surfaces, respectively. As the K_{dc} value increases, the complexity of the vibration spectra at the same finite element point of the core and winding change significantly. The increase in the DC content leads to an increase in the number of secondary frequencies of vibration acceleration, with a significant increase in the frequency doubling peak at 50 Hz and the onset of even frequency peaks. When K_{dc} increases to 1.0, the main frequency position shifts to 250 Hz, and the secondary frequency peaks, except at 100 Hz, increase sharply,

which is closely related to the operating state of the core at this time, with the core approaching saturation. When the K_{dc} value reaches 1.5, the core becomes excessively saturated and the amplitudes of each secondary frequency continue to increase, with the main frequency shifting to 350 Hz. The rightward shift of the main frequency of the two vibrations is related not only to the increased main magnetic flux and leakage harmonic caused by the saturation of the core, but also to the modal vibration mode of the model [34]. As shown in Table I, the main natural frequencies of the model are distributed at 250 Hz and 350 Hz, which directly amplifies the vibration performance under the corresponding excitation.

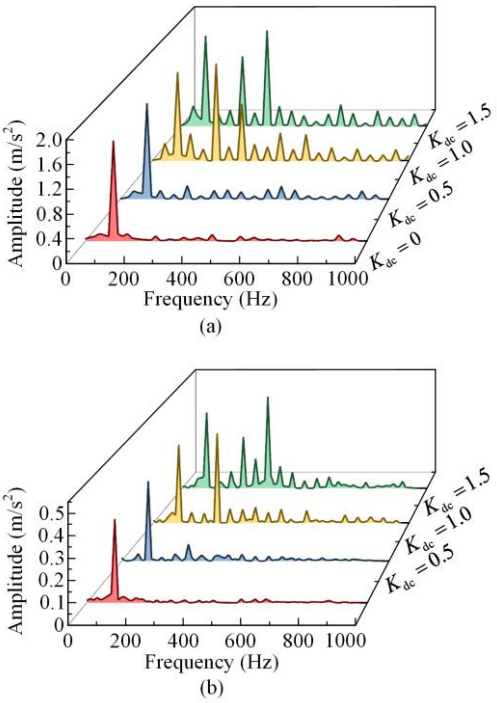

Fig. 7. Frequency domain distribution of vibration acceleration under different DC components. (a) Iron core. (b) Winding.

V. Experimental Analysis

The DC bias experiment on converter transformers is complex and requires two transformers of the same model to form an experimental platform and a large-capacity DC power supply. Therefore, in previous studies, only simulation research is conducted, making it difficult to obtain practical verification of the research conclusions [21], [35]. Derivations are prevalent in some engineering practice theories, particularly regarding the complex structure of converter transformers and the large number of nonlinear phenomena in internal electromagnetic connections. Therefore, corresponding experiments must be designed to verify the reliability of the simulation conclusions. Based on our previous research [36] and the similarity principle, we design and prepare two 1:5 scale model prototypes of the same type of the converter transformer as the experimental platform to further verify the evolution law of the converter transformer vibration characteristics under the DC bias effect, as shown in Fig. 8. DC bias tests are conducted with DC bias coefficients K_{dc}=0, 0.5, 1.0, and 1.5. The high-voltage terminals of the two transformers are connected using corona-free conductors. The rated AC voltage is applied to the low-voltage side of Prototype 1 and directly excites the high-voltage side of Prototype 2 through the high-voltage side of Prototype 1. A DC power supply is connected in series between the neutral points of the two prototypes and an adjustable resistor RT is used to adjust the DC current. The wiring diagram used in the experiment is shown in Fig. 9, where RT refers to the adjustable resistor, B1 denotes the intermediate transformer, T1 is Prototype 1, and T2 is Prototype 2.

The vibration characteristics of the prototype with different DC components are measured and analyzed using an AD-LINK-USB-2405 data acquisition card combined with a YD30 piezoelectric sensor. The distribution of the measurement points is shown in Fig. 10, with six points on the front, two on the side, and two on the top. Points 1–4 primarily reflect the longitudinal vibration perpendicular to the main column and winding of the core, points 7–8 reflect the transverse vibration of the core and winding, and points 9–10 reflect the axial vibration. Generally, owing to the pretightening method of the fasteners, the axial vibration is slightly smaller [37].

Fig. 8. Preparation of scale prototypes.

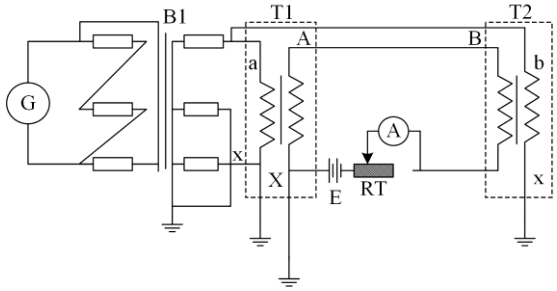

Fig. 9. Wiring diagram for DC bias experiment.

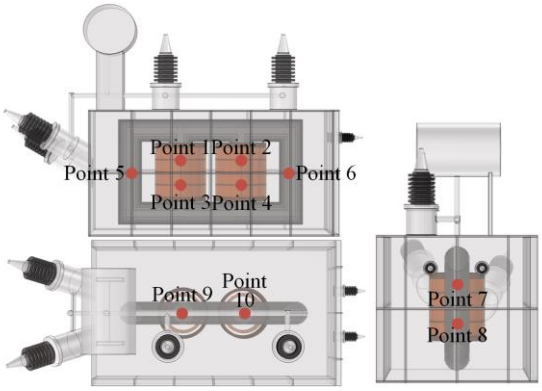

Fig. 10. Description of measurement point location.

The two prototypes are subjected to load tests under different DC components using the post-short-circuit method to determine the winding vibration characteristics under the DC bias effect. Figures 11(a)–(j) present the time-domain diagram of the vibration acceleration of the load experiment at points 1–11 for different DC components. Considering the average value of the vibration acceleration amplitude, K_{dc} increases from 0 to 0.5. The vibration acceleration amplitude of measurement points 1–6 increases by 11.2%, the vibration acceleration amplitude of measurement points 7–8 increases by 10.7%, and the vibration acceleration amplitude of measurement points 9–10 increases by 14.8%. This indicates that the DC bias effect contributes differently to the amplitude and the radial and axial vibrations of the winding. Simultaneously, it can be observed that as the K_{dc} increases, the waveform of vibration acceleration at each measuring point gradually becomes disordered, which corresponds to the increase in harmonic content after adding DC components.

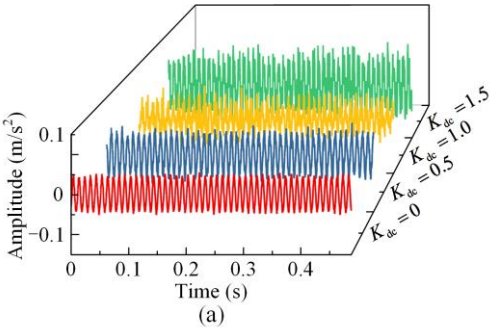

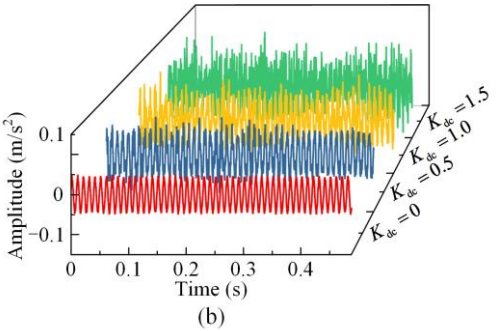

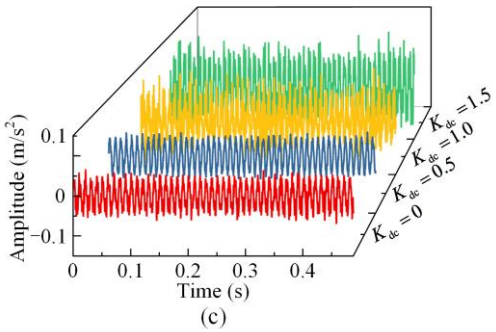

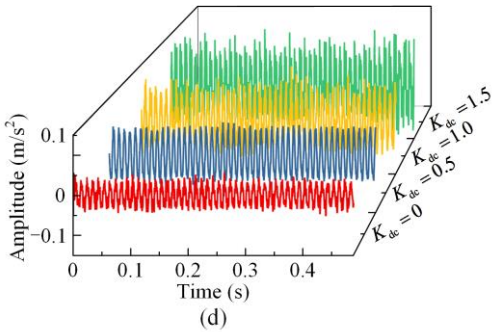

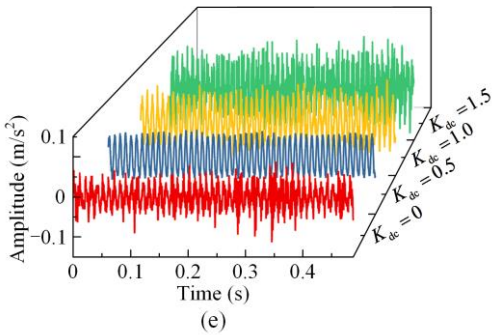

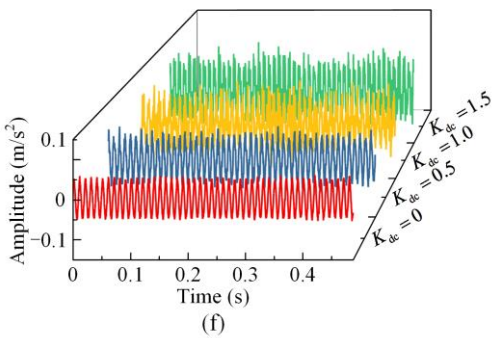

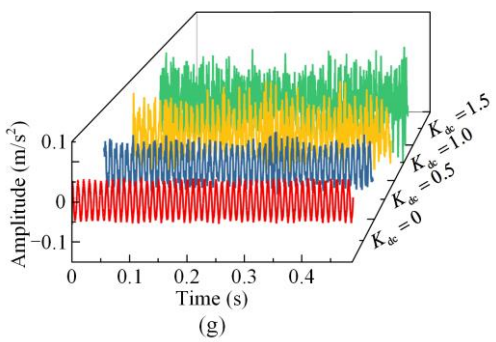

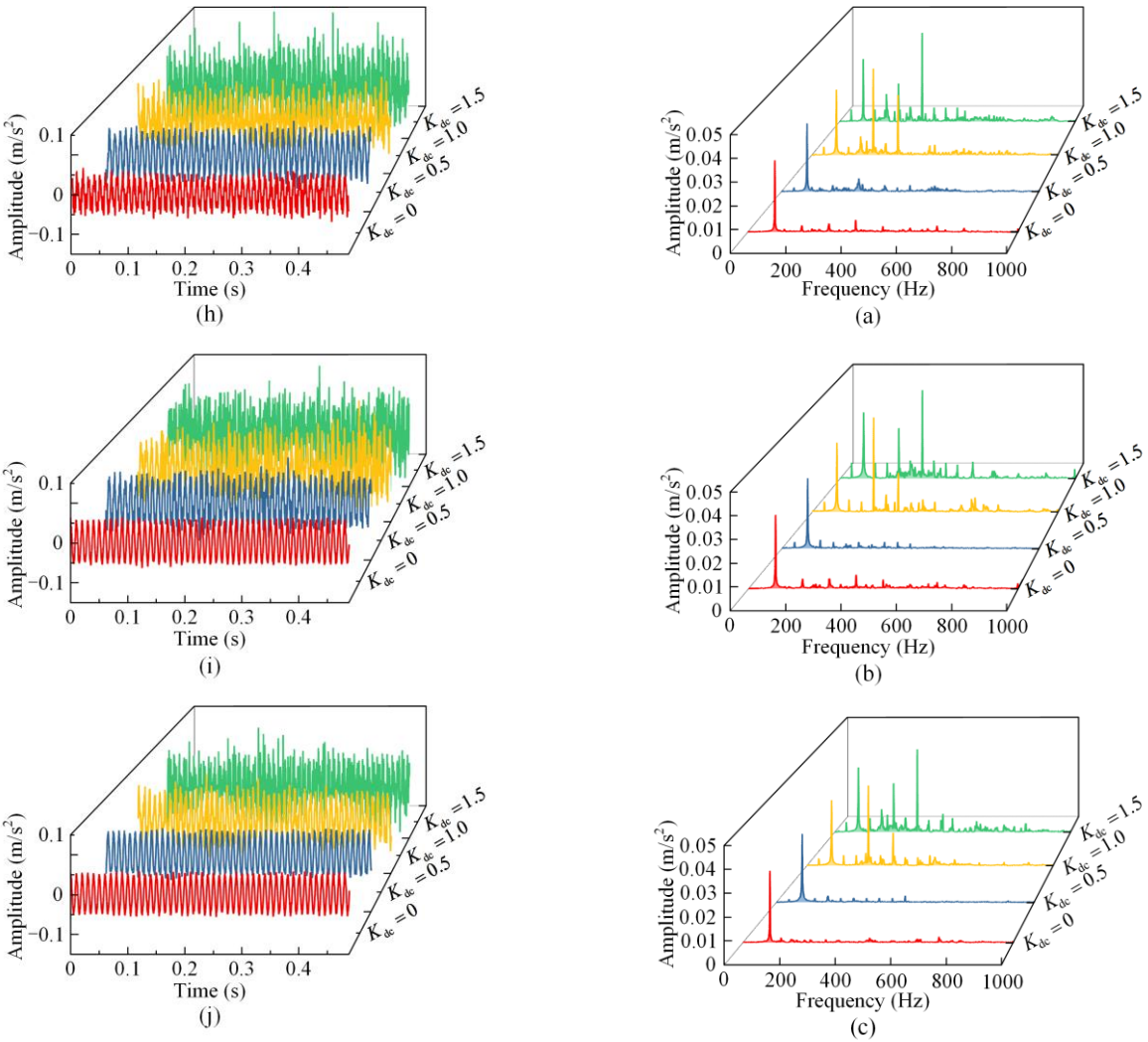

Fig. 11. Time domain distribution of load vibration acceleration under DC bias. (a)–(j) Time-domain distribution of vibration acceleration at measurement points 1–11.

The frequency-domain distribution characteristics of the vibration acceleration in the load experiments at points 1–11 under different DC components are obtained by performing a fast Fourier transform on the time-domain signal of the vibration acceleration, as shown in Figs. 12 (a)–(j). It can be observed from the figures that when K_{dc} increases from 0 to 0.5, the main frequency of the winding vibration remains at 100 Hz, but the frequency distribution increases at 50 octaves, such as 50 Hz, 150 Hz, 250 Hz, 350 Hz, etc., which is similar to the test results in [31]. When K_{dc} increases from 0.5 to 1.0, there is no significant change in the frequency distribution. However, the main frequency increases from 100 Hz to 250 Hz, and the peak acceleration at 350 Hz increases more significantly. When K_{dc} increases from 1.0 to 1.5, and 350 Hz becomes the new dominant frequency, the amplitude of the vibration acceleration remains high at 100 Hz and 250 Hz.

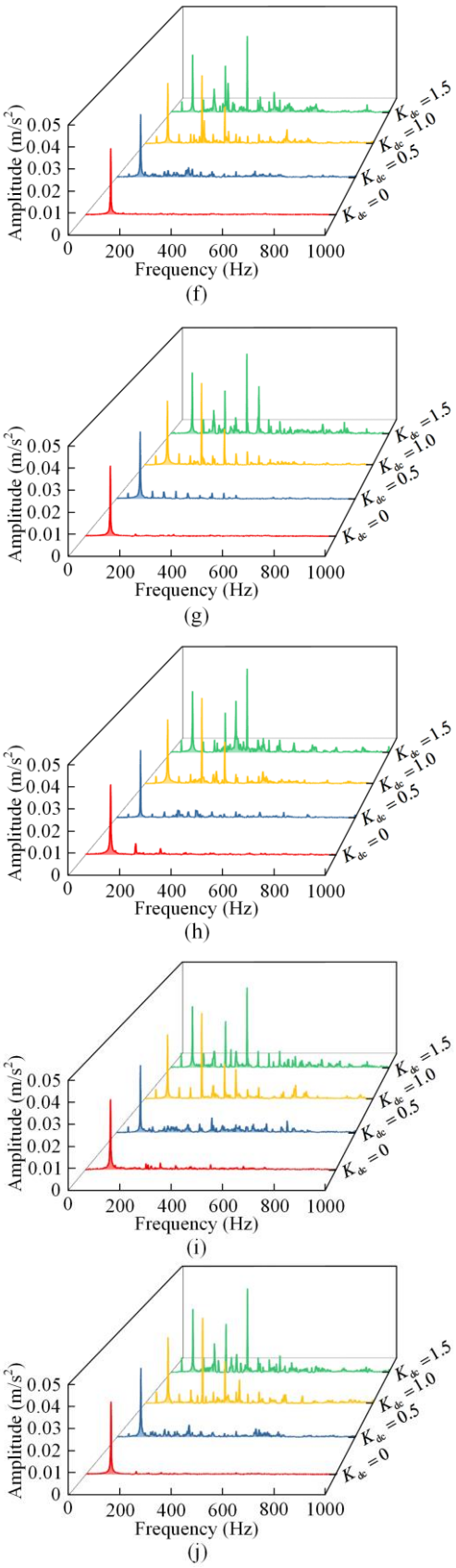

Fig. 12. Frequency domain distribution of load vibration acceleration under DC bias magnetic field. (a)–(j) Frequency domain distributions of vibration acceleration at measurement points 1–11, respectively.

The two prototypes are subjected to no-load tests under different DC components, and the time-domain diagrams of the core vibration characteristics under the DC bias effect are obtained, as shown in Fig. 13. Figures 13 (a)–(j) correspond to measurement points 1–11, respectively. The K_{dc} increased from 0 to 0.5, and the average vibration acceleration amplitude of measurement points 1–6 increased by 13.6%. The vibration acceleration amplitude of measurement points 7–8 increased by 10.7%, and the vibration acceleration amplitude of measurement points 9–10 increased by 8.8%. With the addition of the DC component, the no-load vibration acceleration changes from a neat "rectangle" to a "comb" shape, corresponding to a uniform harmonic growth, a phenomenon that has not been reported previously.

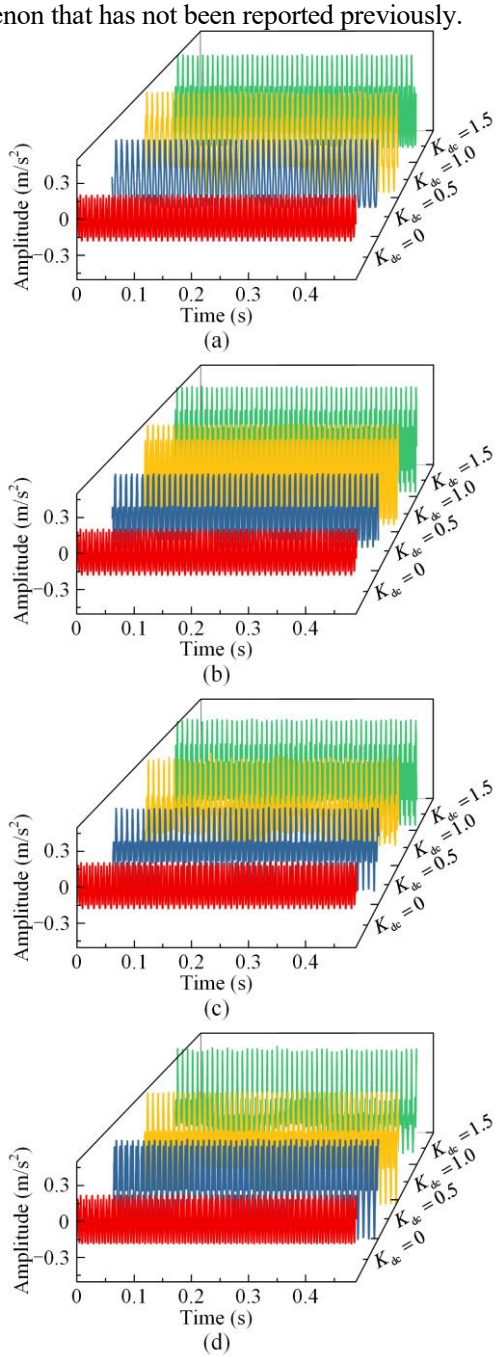

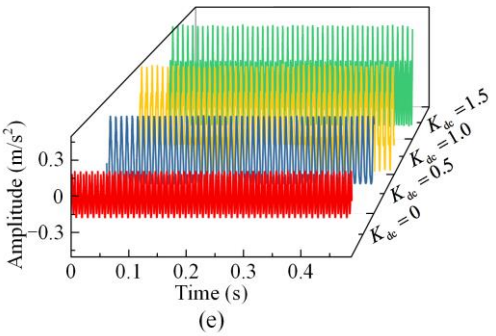

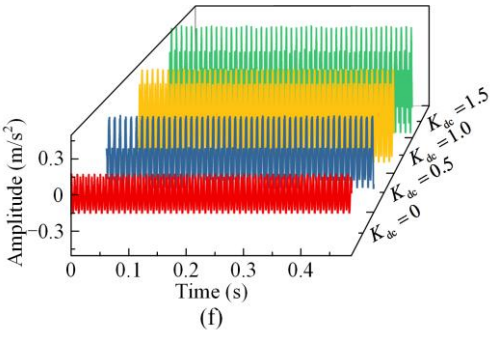

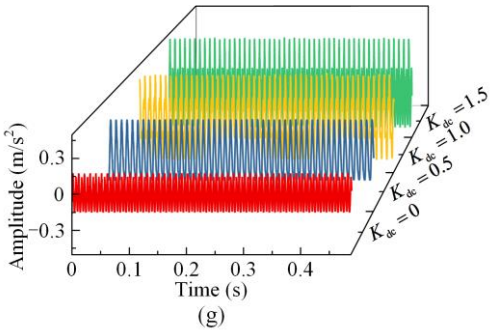

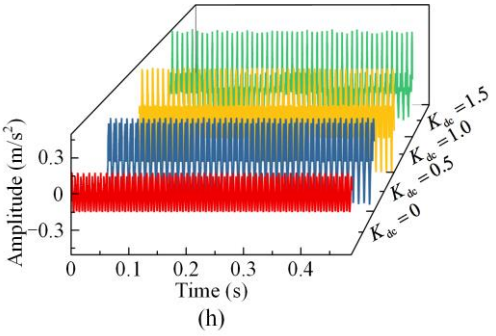

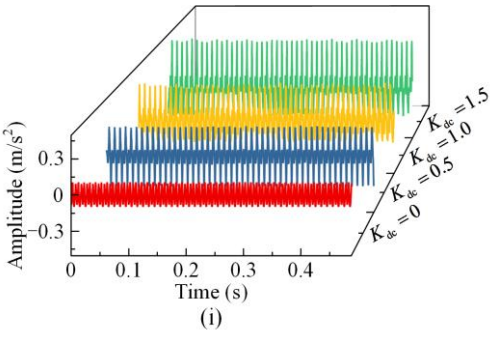

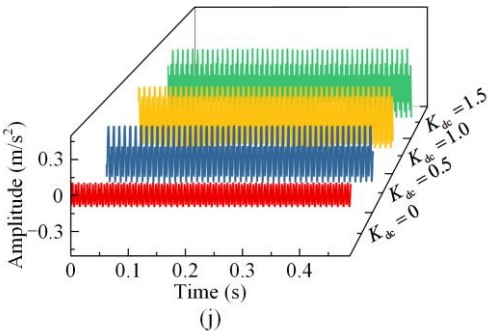

Fig. 13. Time domain distribution of no-load vibration acceleration under DC bias. (a)–(j) Time-domain distribution of vibration acceleration at measurement points 1–11.

Figures 14 (a)–(j) show the frequency-domain distribution characteristics of the load experimental vibration acceleration at measurement points 1–11 for the different DC components. The main frequency band of the core vibration acceleration changes with the DC component, similar to the winding, primarily within a frequency band of 1000 Hz [38]. The frequency doubling of the vibration acceleration at 50 Hz increases with K_{dc}. The main frequencies of the vibration acceleration are 100 Hz, 100 Hz, 250 Hz, and 350 Hz at K_{dc} =0, 0.5, 1.0, and 1.5, respectively. These rules are consistent with the vibration frequency domain characteristics of the core and winding in the simulation at different K_{dc} values.

Based on the simulation and experimental results, it can be concluded that a K_{dc} of 1.0, which is an important reference point, and the corresponding DC content are sufficient to cause the following qualitative changes in the vibration characteristics:

1) Change the working characteristics of core to quickly saturate it, thereby increasing its loss and vibration.

2) Increasing the leakage magnetic field strength of the winding exacerbates winding vibration and increases heat loss.

3) The frequency domain distribution characteristics of the vibration are changed to shift the main frequency of the vibration to the right.

4) The failure of the modal design that intersects with the operating vibration frequency increases the probability of resonance, as indicated in Table I, exacerbating the overall vibration noise.

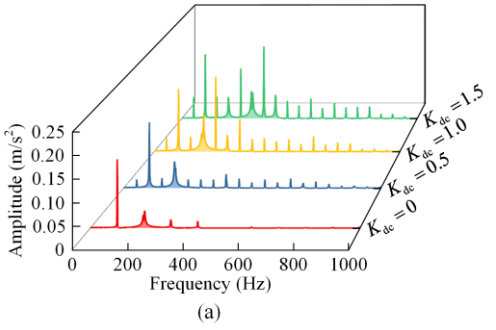

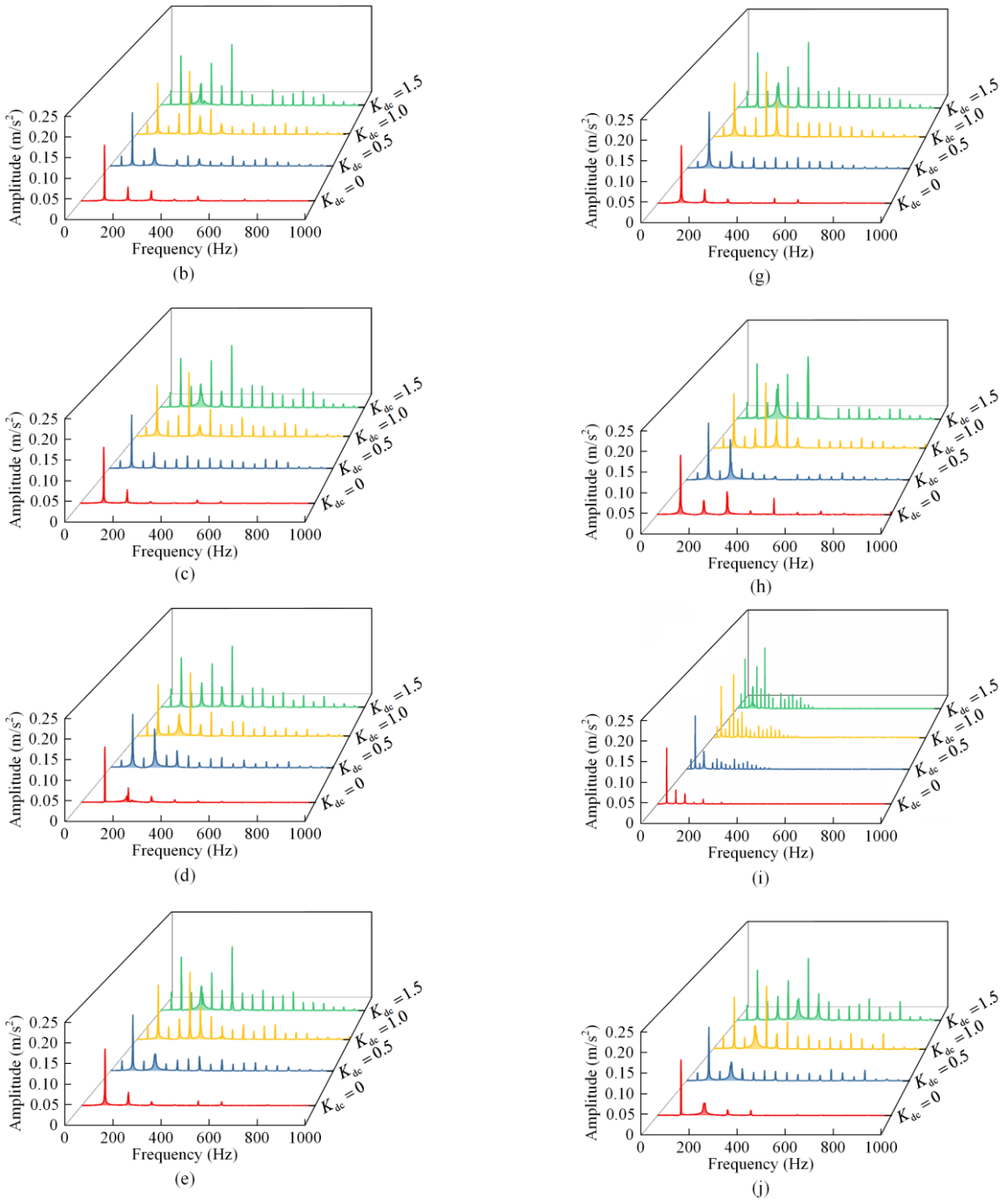

Fig. 14. Frequency domain distribution of no-load vibration acceleration under DC bias magnetic field. (a)–(j) are the frequency domain distributions of vibration acceleration at measurement points 1–11, respectively.

Therefore, based on the experimental conclusions of this paper, it is recommended that the upper limit of the DC content during the operation of the converter transformer should not exceed a K_{dc} of 1.0, and the modal design of the converter transformer should also consider the vibration acceleration peaks at 250 Hz and 350 Hz.

VI. Conclusion

Simulation and experimental platforms for the DC bias of converter transformers are designed and developed using the finite-element method and similarity principle. The vibration, electromagnetic field, and loss characteristics under different K_{dc} values are analyzed, and the following conclusions are drawn:

1) The DC bias increases the harmonic content of the excitation current, primarily manifested as an increase in the even harmonics, resulting in changes in the internal vibration and magnetic characteristics. The DC bias voltage increases the magnetic flux density, vibration, and displacement amplitude of the core and winding, reaching a turning point when K_{dc} is 1.0.

2) As the DC component increases, the core and winding exhibits different vibration and loss characteristics. The K_{dc} value increases from 0.0 to 1.0, the force, loss and displacement of the core and winding are positively correlated; when K_{dc} reaches 1.0, the core approaches the saturation point, at this point, K_{dc} continues to increase, the rate of increase in the main magnetic induction intensity slows down, and the core loss increases sharply, while the leakage flux continues to increase rapidly, exacerbating the winding loss.

3) Under both experimental conditions, the time-domain amplitude growth rate of the vibration acceleration is approximately 10%. The DC bias significantly increases the odd frequency component of the 50 Hz vibration acceleration of the converter transformer. When the DC component reaches a certain proportion, it changes the dominant frequency of the vibration. When K_{dc} reaches 1.0 and 1.5, the main frequencies of the converter transformer become 250 Hz and 350 Hz, respectively.

Acknowledgment

Not applicable.

Authors' Contributions

Hao Wang: writing original draft preparation, review and editing, and formal analysis. Li Zhang: conceptualization, resources, data curation, supervision, and project administration. Youliang Sun: validation, investigation, visualization, and funding acquisition. Liang Zou: methodology and software. All authors have read and agreed to the published version of the manuscript.

Funding

This work is supported by the Key R&D Program of Shandong Province (No. 2021CXGC010210).

Availability of Data and Materials

Please contact the corresponding author for data material request.

Declarations

Competing interests: The authors declare that they have no known competing financial interests or personal relationships that could have appeared to influence the work reported in this article.

Authors' Information

Hao Wang is currently pursuing a doctoral degree at Shandong University. His main research areas are power equipment operation protection and new electrical materials.

Li Zhang is a professor and doctoral supervisor at Shandong University. His research focuses on applied electromagnetics and high-voltage electrical equipment.

Youliang Sun is a professor level senior engineer, chief engineer of transformer preparation company, mainly focuses on the design, preparation, and operation and maintenance of high-capacity transformers.

Liang Zou is a professor at the School of Electrical Engineering, Shandong University, mainly engaged in research on protection and control of large-scale power equipment, and modification design of high-frequency insulation materials.

References

[1] T. Hammons, D. Woodford, and J. Loughtan *et al*., "Role of HVDC transmission in future energy development," *IEEE Power Engineering Review*, vol. 20, no. 2, pp. 10-25, Feb. 2000.

[2] C. Kim, G. Jang, and V. Sood *et al*., "HVDC transmission: power conversion applications in power systems," *Wiley-IEEE Press*, 2009.

[3] M. Mohan, "A comprehensive review of DC fault protection methods in HVDC transmission systems," *Protection and Control of Modern Power Systems*, vol. 6, no. 1, pp. 1-20, Jan. 2021.

[4] B. Yang, B. Liu, and H. Zhou, "A critical survey of technologies of large offshore wind farm integration: summary, advances, and perspectives," *Protection and Control of Modern Power Systems*, vol. 7, no. 2, pp. 233-264, Apr. 2022.

[5] B. Du, Q. Wang, and Y. Tu, *et al*., "Guest editorial: advanced materials for HVDC insulation," *High Voltage*, vol 5, no. 4, pp. 351-352, Oct. 2020.

[6] W. Xie, F. Xiao, and C. Tu *et al*., "Suppression strategy for the inrush current of a solid-state transformer caused by the reclosing process," *Protection and Control of Modern Power Systems*, vol 8, no. 4, Oct. 2023.

[7] Q. Li, Q. Chen, and J. Wu *et al*., "Ensemble learning-based HVDC systems fault diagnosis," *Power System Protection and Control*, vol. 51, no. 16, pp. 168-178, Aug. 2023. (in Chinese)

[8] F. Ahsan, N. Dana, and S. Sarker *et al*., "Data-driven next-generation smart grid towards sustainable energy evolution: techniques and technology review," *Protec-*

tion and Control of Modern Power Systems, vol. 8, no. 3, pp. 1-42, Jul. 2023.

[9] W. Wu, W. Zhang, and Z. Xiao *et al*., "Parameter optimization design of a CLLC resonant converter based on time domain analysis," *Power System Protection and Control*, vol. 51, no. 14, pp. 139-151, Jul. 2023. (in Chinese)

[10] Y. Zhao and P. Crossley, "Impact of DC bias on differential protection of converter transformers," *International Journal of Electrical Power & Energy Systems*, vol. 115, pp. 105426, Feb. 2020.

[11] Q. Wang, P. Liu, and H. Tian *et al*., "Research on the dynamic characteristics of electric field distribution of the ± 1100 kV ultra high voltage converter transformer valve-side bushing using weakly ionized gas conductance model," *High Voltage*, vol. 7, no. 2, pp. 288-301, Apr. 2022.

[12] S. Chen, A. Wood, and J. Arrilwxlaga *et al*., "HVDC converter transformer core saturation instability: a frequency domain analysis," *IEE Proceedings-Generation, Transmission and Distribution*, vol. 143, no. 1, pp. 75-81, Jan. 1996.

[13] P. Shao, L. Luo, and Y. Li *et al*., "Electromagnetic vibration analysis of the winding of a new HVDC converter transformer," *IEEE Transactions on Power Delivery*, vol. 27, no. 1, pp. 123-130, Jan. 2012.

[14] S. Yadav and R. Mehta, "Modelling of magnetostrictive vibration and acoustics in converter transformer," *IET Electric Power Applications*, vol. 15, no. 3, pp. 332-347, Mar. 2021.

[15] Y. Chen, W. Fu, and H. Lin *et al*., "A passive negative magnetic reluctance structure-based kHz transformer for improved DC magnetic bias withstanding," *IEEE Transactions on Power Electronics*, vol. 38, no. 1, pp. 717-727, Jan. 2023.

[16] T. Wang, K. Chen, and K. Zhang *et al*., "Research and analysis on suppression and influence of transformer direct current bias," *Journal of Physics: Conference Series*, vol. 2369, pp. 012049, 2022.

[17] S. Canturk, M. Balci, and M. Hocaoglu *et al*., "Performance analysis of three-phase five-leg transformers under DC bias using a new frequency-dependent reluctance-based model," *IET Generation*, *Transmission & Distribution*, vol. 12, no. 16, pp. 2455-2465, 2022.

[18] A. Moses, P. Anderson, and T. Phophongviwat, "Localized surface vibration and acoustic noise emitted from laboratory-scale transformer cores assembled from grain-oriented electrical steel," *IEEE Transactions on Magnetics*, vol. 52, no. 10, pp. 1-15, Oct. 2016.

[19] A. Sayed, M. Abouelatta, and M. Badawi *et al*., "Novel accurate modeling of dust loaded wire-duct precipitators using FDM-FMG method on one fine computational domains," *Electric Power Systems Research*, vol. 203, pp. 107634, Feb. 2022.

[20] A. S. Zalhaf, D. E. A. Mansour, and Y. Han *et al*., "Numerical and experimental analysis of the transient behavior of wind turbines when two blades are simultaneously struck by lightning," *IEEE Transactions on Instrumentation and Measurement*, vol. 71, pp. 1-12, 2022.

[21] H. Wang, Q. Yang, and Y. Li *et al*., "Numerical analysis of the influence of magnetic shielding on stray losses and temperature rise in adjacent parts of transformer ascending flange," *IEEE Transactions on Applied Superconductivity*, vol. 31, no. 8, pp. 1-4, Nov. 2021.

[22] X. Zhang, X. Liu, and F. Guo *et al*., "Calculation of DC bias reactive power loss of converter transformer via finite element analysis," *IEEE Transactions on Power Delivery*, vol. 36, no. 2, pp. 751-759, Apr. 2021.

[23] K. Dawood, G. Komurgoz, and A. Koseoglu *et al*., "Design optimization for distance between additional and tap winding in high voltage transformers," *High Voltage*, vol. 5, no. 6, pp. 716-723, Dec. 2020.

[24] R. Barros, E. Costa, and J. Araujo *et al*., "Contribution of inrush current to mechanical failure of power transformers windings," *High Voltage*, vol. 4, no. 4, pp. 300-307, Dec. 2019.

[25] Z. Pu, J. Ruan, and Z. Du *et al*., "Analysis of voltage distribution characteristics in UHVDC converter transformer winding based on the reduced-scale model," *IEEE Transactions on Magnetics*, vol. 50, no. 11, pp. 1-5, Nov. 2014.

[26] B. Garcia, J. C. Burgos, and A. M. Alonso, "Transformer tank vibration modeling as a method of detecting winding deformations-part II: experimental verification," *IEEE Transactions on Power Delivery*, vol. 21, no. 1, pp. 164-169, Jan. 2006.

[27] K. Srishail, R. Sachin, and H. Pradeepa *et al*., "Grid power quality enhancement using an ANFIS optimized PI controller for DG," *Protection and Control of Modern Power Systems*, vol. 7, no. 1, pp. 26-39, Jan. 2022.

[28] X. Zhao, Y. Du, and Y. Liu *et al*., "Magnetostrictive properties of the grain-oriented silicon steel sheet under DC-biased and multisinusoidal magnetizations," *Materials*, vol. 12, no. 13, pp. 1-15, 2019.

[29] L. Zeng, Z. Zhu, and B. Bai *et al*., "Research on influence of DC magnetic bias on a converter transformer," in *2007 International Conference on Electrical Machines and Systems*, Seoul, Korea, Dec. 2007, pp. 1346-1349.

[30] X. Cheng, Y. Ni, and K. Yu *et al*., "Analysis on harmonic characteristic of transformer DC bias caused by metro stray current," *Journal of Physics: Conference Series*, vol. 2196, no. 1, pp. 012014, Jan. 2022.

[31] Y. Tong, Q. Zhu, and L. He, "Analysis on DC bias impact on converter transformers operation," *High Voltage Engineering* , vol. 47, no. 6, pp. 2206-2213, Jun. 2021. (in Chinese)

[32] H. Sung and C. Jae, "Saturation characteristic of iron core dependent on fault angle in a flux-lock type SFCL," *Journal of the Korean Institute of Illuminating and Electrical Installation Engineers*, vol. 21, no. 10, pp. 029, 2007.

[33] B. Garcia, J. C. Burgos, and A. M. Alonso, "Transformer tank vibration modeling as a method of detecting winding deformations-part I: theoretical foundation," *IEEE Transactions on Power Delivery*, vol. 21, no. 1, pp. 157-163, Jan. 2006.

[34] H. Dulabhai, V. Singh, and M. Yadav, "Analysis of natural frequency for three-dimensional model of transformer winding using FEA," vol. 8, no. 1, Jan. 2018.

[35] X. Li, X. Wen, and P. N. Markham *et al*., "Analysis of nonlinear characteristics for a three-phase, five-limb transformer under DC bias," *IEEE Transactions on Power Delivery*, vol. 25, no. 4, pp. 2504-2510, Oct. 2010.

[36] H. Wang, L. Zhang, and Y. Sun *et al*., "Vibration scale model of a converter transformer based on the finite element and similarity principle and its preparation," *Processes*, vol. 11, no. 7, Jun. 2023.

[37] Y. Hori and K. Okuyama, "Axial vibration analysis of transformer windings under short circuit conditions," *IEEE Transactions on Power Apparatus and Systems*, vol. PAS-99, no. 2, pp. 443-451, Mar. 1980.

[38] R. Xiao, Z. Zhang, and Y. Wu, "Multi scale information fusion model for feature extraction of converter transformer vibration signal," *Measurement*, vol. 180, no. 3, pp. 109555, Aug. 2021.